
VIRUS TRANSMISSION BY AEROSOL TRANSPORT DURING SHORT CONVERSATIONS

A PREPRINT

Rohit Singhal

Department of Aerospace Engineering,
Indian Institute of Science,
Bengaluru 560012
rohitsinghal@iisc.ac.in

S. Ravichandran

Nordic Institute for Theoretical Physics,
KTH Royal Institute of Technology and Stockholm University,
Stockholm, 10691-SE
ravichandran@su.se

Rama Govindarajan

International Centre for Theoretical Sciences,
Bengaluru 560089
rama@icts.res.in

Sourabh S. Diwan *

Department of Aerospace Engineering,
Indian Institute of Science,
Bengaluru 560012
sdiwan@iisc.ac.in

March 1, 2025

ABSTRACT

The airborne transmission of disease-causing pathogens like the SARS-CoV-2 virus responsible for the COVID-19 pandemic is known to occur not only through violent expiratory events like coughs or sneezes, but also during activities like singing and even speech. We study, using direct numerical simulation (DNS), the transport of virus-laden aerosols generated during human speech. We show that the use of the “top-hat” formulation for steady speech flows can underestimate infection probabilities by a factor of 2-3. We propose an alternative method of estimating viral ingestion that includes exposure through the eyes and mouth, to provide more realistic estimates of the risk of infection. This method is then used to determine infection probabilities when two speakers facing each other are engaged in a short conversation. We show that the interaction between the two oppositely-directed speech jets can increase or decrease infection probabilities, which peak for a height difference between the speakers of about 10cm (30cm) when the axial separation between them is 2ft (6ft). These results can help improve the existing public health guidelines for COVID mitigation by introducing a lateral shift between people during short conversations. Moreover, simulations like these can provide useful inputs to the existing epidemiological models for improving their reliability and accuracy.

Keywords SARS-CoV-2 · Speech flow · Direct numerical simulations · Conversation · Aerosol transport

1 Introduction

The mode of transmission of the virus SARS-CoV-2, responsible for the COVID-19 pandemic, has been a matter of debate. Around the beginning of the pandemic in early 2020, the primary source of the spread of infection was believed to be the “direct” droplet transmission, in which the droplets released by an infected symptomatic person (through events like coughing, sneezing etc.) come in direct contact with a susceptible person. An indirect virus transmission through fomites was also considered (<https://www.who.int/news-room/q-a-detail/q-a-coronaviruses>). Based on the former mode of transmission, WHO recommended maintaining a physical distance of 1m between people to minimize the spread of infection, whereas the recommendation of CDC-USA is a separation distance of 6ft. By mid-2020, it became clear that an asymptomatic person too can cause COVID transmission through the release of virus-laden droplets while talking, breathing etc., and this was believed to be responsible for the rapid spread of the disease in the mid to late

*Corresponding author

2020 [1, 2]. It was thus realised that public health measures such as masking and social distancing would be necessary when an infected person (symptomatic or asymptomatic) merely engages in a conversation with another person and not just during more violent expiratory events such as coughing/sneezing [1]. These findings highlighted the need to better understand the different transmission modes of SARS-CoV-2, in which the fluid dynamics of droplet/aerosol transport plays a key role [3]. In particular, the scientific attention was focused on the fact that the social distancing guidelines set out in most public health advisories were based on an arbitrary distinction between ‘small’ and ‘large’ respiratory droplets drawn in a study dating from the 1930s [4]. The study showed that larger droplets ($> 100\mu m$) settle faster than they evaporate but can cover 1-2m horizontally while doing so, causing direct transmission, whereas smaller droplets evaporate faster than they settle and therefore do not cause direct transmission. Recent research has shown that this distinction between ‘small’ and ‘large’ droplets is arbitrary and there is an entire spectrum of droplet sizes released during different expiratory events and that these droplets can be transported over long distances by the turbulent jet/puff generated during these events [3]. As a result moderate to small sized droplets can remain suspended in the air and cause airborne transmission. The complexity of the transmission dynamics of SARS-CoV-2, coupled with its asymptomatic transmissibility, could thus have played a large role in the ongoing pandemic afflicting the world [5].

The virus-laden droplets responsible for disease transmission are generated in the nasopharyngeal tract. Bourouiba [3] discusses the break-up of mucosalivary fluid bubbles and the formation of the droplets ranging from $1\mu m$ to $500\mu m$ [6, 7]. The survival times for the virus inside large droplets that predominantly contaminate surfaces close to the source (including the nasopharyngeal tract of a susceptible person) have been studied (see, e.g., [8, 9]); the typical half life of SARS-CoV-2 in such droplets is found to be about 15 minutes [10, 11]. As mentioned earlier, small droplets can stay airborne for long times, with their longevity a function both of their composition and of the prevalent ambient conditions like the relative humidity and the temperature. Furthermore, the small droplets can evaporate completely while airborne and turn into what are called droplet nuclei. The half-life of SARS-CoV-2 on the dried droplet nuclei is not known but there is evidence that the virus survives within such nuclei [12]. The long-range transport of disease causing viruses through such droplets and droplet nuclei, and the impact of the ambient conditions on virus survival, are open questions of fluid dynamical interest [13], with some studies suggesting that droplets with diameters in the range of $(2.5\mu m - 19\mu m)$ have the greatest potential for causing the initial nasopharyngeal infection [14, 13, 15]. The size of droplets is also a function of the kind of respiratory flow. Coughs and sneezes, which are violent expiratory events, are known to produce droplets with a broad size distribution ranging from $1\mu m$ to more than $100\mu m$ [7], whereas the droplets exhaled while speaking are typically smaller than $\approx O(10\mu m)$ [16]. Thus the droplets emitted during speech could be among the most dangerous to cause COVID-19 infection and need a careful characterization.

The transport of droplets in flows generated by coughing and sneezing have been studied in the past; see [17, 18, 19]. Flow visualisations using the Schlieren technique [20, 21] confirm the basic understanding of droplet dynamics outlined above, with realistic geometries studied using mannequins [22]. Attempts have been made to model the behaviour of respiratory droplets for incorporating them in epidemiological models to improve their prediction accuracy [8, 23, 24].

Most numerical studies on respiratory flows have used flow models such as the Reynolds-averaged Navier Stokes equations with Lagrangian tracking of the respiratory particles [25, 26, 27]. One such study [28] provides a risk assessment of virions exhaled due to normal breathing in elevators, classrooms, and supermarket settings. The increasing availability of computing power has made direct numerical simulations (DNS) of such flows feasible (although only for idealised geometries). Chong et al. [29] studied the effect of relative humidity and temperature on the droplets, finding that droplets can last $O(100)$ times longer in cold humid air than predicted by classical models [4]. Rosti et al. [30] carried out a DNS for cough and sneeze flows and showed that droplet evaporation time is controlled by the combined effects of turbulence and droplet inertia. They also estimated the errors that could be introduced into these calculations due to the coarse-graining effect of flow models. Another recent study [31] has performed DNS on a mild cough flow to track the trajectory of the leading vortex ring and investigate its three-dimensional structure.

Cough and sneeze flows have received considerable attention since the start of the pandemic, but there have been fewer investigations on the fluid dynamics of speech. Experiments on the effects of airflow velocity on droplet trajectory in speech and vocal exercises have been used to construct models of the behaviour of small and large droplets [32]. Abkarian et al. [33] carried out a large eddy simulation (LES) of speech flows generated by repetition of certain phrases. They showed that beyond a certain distance from the mouth of the speaker, the speech flow starts behaving like a steady jet that spreads at typical half-angles of $10^\circ - 14^\circ$. Furthermore, they found that the reach of the flow is proportional to the square root of time, as is expected for steady jets. These results were incorporated by Yang et al. [34] in a simplified model for the transport of aerosol particles away from a speaker’s mouth, using the $1/x$ variation of the velocity and scalar concentration typical of a steady jet; x being the axial distance. They calculated the probability of infection of a silent listener based on conservative estimates of the minimum number of virions ($N_{inf} \approx 100$) that must be inhaled to cause infection [14, 35] and presented space-time maps of the risk of infection. This study highlighted the fact that airborne infections involve not just distances but also time durations of exposure (see also [36]) and that these should also be incorporated in public health guidelines.

The present study is devoted to gauging infection probability during a conversation between two people. The idealised scenario where a single speaker engages in an extended monologue is of limited applicability, and typical conversations are dialogues of limited time spans (e.g. at a supermarket counter). We report results from a parametric study of the concentration profiles and the resultant infection probabilities in the flows associated with such short conversations. Our results offer interesting experimental test cases, and can be used as the basis for models in future studies. We show that the approximation of speech flows as steady jets can underestimate infection probabilities and propose an alternative method of estimating viral exposure that includes exposure through the eyes and mouth. We then estimate, using this method, infection probabilities when two speakers facing each other are engaged in conversation. We find that the speech jet emanating from the second speaker significantly alters the evolution of the jet from the first speaker. For a given axial separation between the two speakers we find that the probability of infection peaks when the vertical (or lateral separation) between them is about 0.1 to 0.2 times the separation distance. We also discuss the implications of these results towards improving the social distancing guidelines and towards epidemiological modelling.

The rest of the paper is organised as follows. In Section 2, we write down the governing equations, and provide details of the numerical solver used. We then validate the solver by comparing our results against the steady jet prediction of Abkarian et al. [33], and against the model of Bourouiba et al. [18] where buoyancy forces become important. In Section 3.1, we revisit the single-speaker case, showing in Sec. 3.1.2 how previous calculations underestimate infection probability by using a top-hat instead of a Gaussian radial profile for quantities associated with the steady jet. We propose a new method of calculating viral exposure in Sec. 3.1.3. In Section 3.2, we set up and study the case of conversations involving two speakers, estimating infection probabilities using the method proposed in Sec. 3.1.3. We conclude in Section 5 with thoughts on the limitations of studies such as the present one and ideas for future studies.

2 Problem Setup

2.1 Geometry and Governing Equations

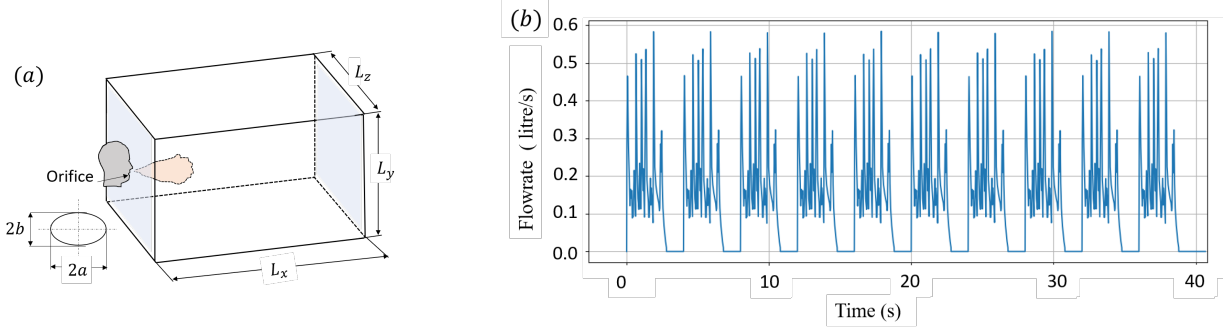


Figure 1: (a) Schematic of our cuboidal simulation domain for the single-speaker case, with speech flow from an imaginary speaker at the left face. The person's mouth is modeled as an orifice of elliptic cross-section. (b) Flow rate prescribed at the orifice, consisting of 10 identical cycles each with a spoken phrase (of 2.8s) with a halt of 1.2s.

Our domain of interest is a cuboidal volume of dimensions L_x, L_y, L_z along the three coordinate axes, as sketched in Fig. 1(a). Here x, y, z are the axial, vertical (against gravity) and lateral co-ordinates respectively. The human mouth is modelled as an elliptical orifice on one of the walls of the domain, with major and minor axes of length $a = 1.5\text{cm}$ and $b = 1.0\text{cm}$ respectively, following Abkarian et al. [33]. We use the characteristic diameter $d = 2\sqrt{ab} = 2.45\text{cm}$ of the ellipse as the length-scale for non-dimensionalisation (see below). Abkarian et. al. [33] show that speech phrases with plosive sounds (*oshtavya* in Sanskrit, like words containing the letter 'P') induce puffs that travel further than those having fricative sounds (the letter 'S'). We prescribe the inlet velocity at the orifice using laboratory measurements of flow velocity associated with repeated utterance of the phrase "Peter Piper picked a peck" (see Fig. 4(c) of [33]). The inlet velocity time-series in [33] uses equal volumes (0.5 litres) of exhalation and inhalation and generate a train of puffs. Note that the inhalation acts like a sink and sucks in air from all the directions whereas the exhalation creates a directed jet. The inhalation phase therefore does not affect the speech flow at sufficient distances away from the mouth, as also discussed in [33]. Therefore in the present work we set the inlet velocity to zero during the inhalation phase (figure 1). We show that this does not affect the speech flow significantly, by comparing our results with the simulations of [33] (figure 2). A single 'cycle' of the specified phrase used here has an exhalation part lasting 2.8 seconds, followed by 1.2 seconds with zero inlet velocity. We simulate ten such cycles, amounting to a total of 40 seconds, as shown in Figure 1(b). The maximum flow velocity at the orifice, $u_c = 1.167\text{ m/s}$, is used as the velocity scale. Since these flow

speeds are small compared to the speed of sound in air and also because the imposed temperature difference is small, we make the Boussinesq approximation, and assume that the velocity fields of interest are incompressible, with density differences (proportional to temperature differences) appearing only in the buoyancy term (Eq. 2).

The human body is typically warmer than the ambient air indoors. We therefore allow for the local temperature T in the flow to be a function of space and time, although we find that the resulting buoyancy does not affect the dynamics significantly. The temperature T is nondimensionalised using the characteristic temperature difference $\Delta T_o = T_o - T_{amb} = 14^\circ\text{C}$ between the air expelled from the orifice, T_o , and the ambient temperature T_{amb} .

In order to model the dynamics of the virus laden droplets generated during speech, we make two simplifications. First, the typical size of the droplets ($\mathcal{O}(1 - 10\mu\text{m})$; see Sec. 1) produced during speech are small enough that they follow fluid streamlines. This behaviour can be quantified in terms the Stokes number of the droplets, defined as the ratio τ_p/τ_f , where τ_p is the timescale on which the velocity of the droplets adjusts to the local fluid velocity, and $\tau_f = d/u_c$ is the flow timescale. For droplet sizes typical of speech flows, the Stokes numbers are smaller than 0.1. This allows us to represent the droplets by a scalar field (C_s) that is advected with the flow velocity, with unit concentration at the orifice by definition. This approach has been used before for studying the interaction of droplets and turbulence in a cloud flow [37]. Secondly, we note (a) that the total liquid content in these flows is quite small [16], as are the temperature changes resulting from droplet evaporation; and (b) that the half-life of SARS-CoV-2 in aerosol droplets/nuclei ($\approx 15\text{mins}$) is much longer than the time-scales of evaporation (of the order of seconds). We therefore ignore the thermodynamics of evaporation in this study, thus treating small droplets and aerosol nuclei as interchangeable, both passively advected by the flow. Note that this is consistent with the formulation used in [33] and [34], who did not consider evaporation in analysing speech flows.

The resulting Boussinesq Navier-Stokes equations, with scalar transport equations for temperature and droplet concentration, are

$$\vec{\nabla} \cdot \vec{u} = 0, \quad (1)$$

$$D\vec{u}/D\tilde{t} = -\vec{\nabla}\tilde{p} + \frac{1}{Re}\vec{\nabla}^2\vec{u} + \frac{1}{Fr^2}\theta e_y, \quad (2)$$

$$D\tilde{\theta}/D\tilde{t} = \frac{1}{Re \cdot Pr}\vec{\nabla}^2\tilde{\theta}, \quad (3)$$

$$D\tilde{C}_s/D\tilde{t} = \frac{1}{Re \cdot Sc}\vec{\nabla}^2\tilde{C}_s, \quad (4)$$

where \vec{u} is the fluid velocity, \tilde{p} is the pressure, $\tilde{\theta}$ is the temperature difference between the flow and the ambient, \tilde{C}_s is the passive scalar concentration, $D/D\tilde{t}$ is the material derivative, $Re = u_c d/\nu$ is the Reynolds number, $Fr^2 = u_c^2/dg\Delta T_o$ is the Froude number squared, ν is kinematic viscosity of air and g is acceleration due to gravity, and non-dimensional quantities are represented by a tilde. The governing parameters are the Prandtl number, Pr , and the Schmidt number Sc governing the diffusion of the temperature and the scalar respectively, which are both assigned unit values. For the length and velocity scales mentioned above, characteristic of respiratory flow, $Re = 1906$ and $Fr^{-2} = 0.00842$.

The governing equations (1-4) are solved using the finite-difference DNS solver, Megha-5, which has been previously used in studies of jets & plumes [38] and cumulus & mammatus clouds [37]. The code discretizes the governing equations in a Cartesian geometry using a second-order scheme in space and uses a second-order accurate Adams-Bashforth scheme for time-stepping. For the validation exercise presented in the next subsection, a domain size $L_x = L_y = L_z = 70d = 1.715\text{m}$ is chosen such that the boundaries do not affect the flow in the interior. The orifice with the prescribed inlet velocity is located on the boundary at $x = 0$, as shown in Figure 1(a); at the orifice, $\theta = 1$ by definition, and we set $C_s = 1$. As in previous studies [37, 38] using the same solver, simple open boundary conditions are imposed on the four lateral boundaries at $y = 0, L_y$ and $z = 0, L_z$ and the boundary at $x = L_x$; this enables advection of the turbulent structures out of the domain, without much affecting the upstream flow. The boundary condition at $x = L_x$ is modified when there are two speakers (see Sec. 3.2). Finally, as in Abkarian et al. [33], we assume poor ventilation and no externally imposed mean flow.

2.2 Validation

We validate our simulations by comparing our results to those obtained by Abkarian et al. [33]. We test the convergence of the results obtained by performing the same simulations with three different grids, i.e., 256^3 , 512^3 and 1024^3 (and a CFL number of 0.15 for the appropriate timestep). We also simulate a case of a cough flow and compare it with the experimental results from Bourouiba et al. [18]. The flow generated by multiple successive speech cycles is intermediate between a steady jet and a transient momentum flow (a ‘‘puff’’). Abkarian et al. [33] have shown that at initial times, the flow resembles a puff, but after a few cycles, the ‘‘cycle-averaged’’ centreline velocity follows the standard $1/x$ profile for a steady turbulent jet, as shown in Fig. 2 (a), (b) and (c).

We note that the overall shape of the cycle-averaged curves in our simulations match those that are presented in Abkarian et al. [33] (not shown here), with the averaged velocity following a $1/x$ variation after $x \approx 0.3 - 0.4$, which again is in good agreement with Abkarian et al. [33]. Figure 2(d) shows that the effect of change in the number of grid points 1024^3 to 256^3 is not significant; there is a slight underestimation of the computed velocity in the region $x = 0.2 - 0.4$ for grid 256^3 . However, since we are primarily interested in the aerosol transport over distances $\geq 0.6\text{m}$ (which is the smallest domain size for the conversation simulations presented in section 3.2), and since the reduction in computational cost is significant ($\approx 256\times$ between the highest and lowest resolution), we use a grid-resolution of 256^3 to perform the parametric study reported here.

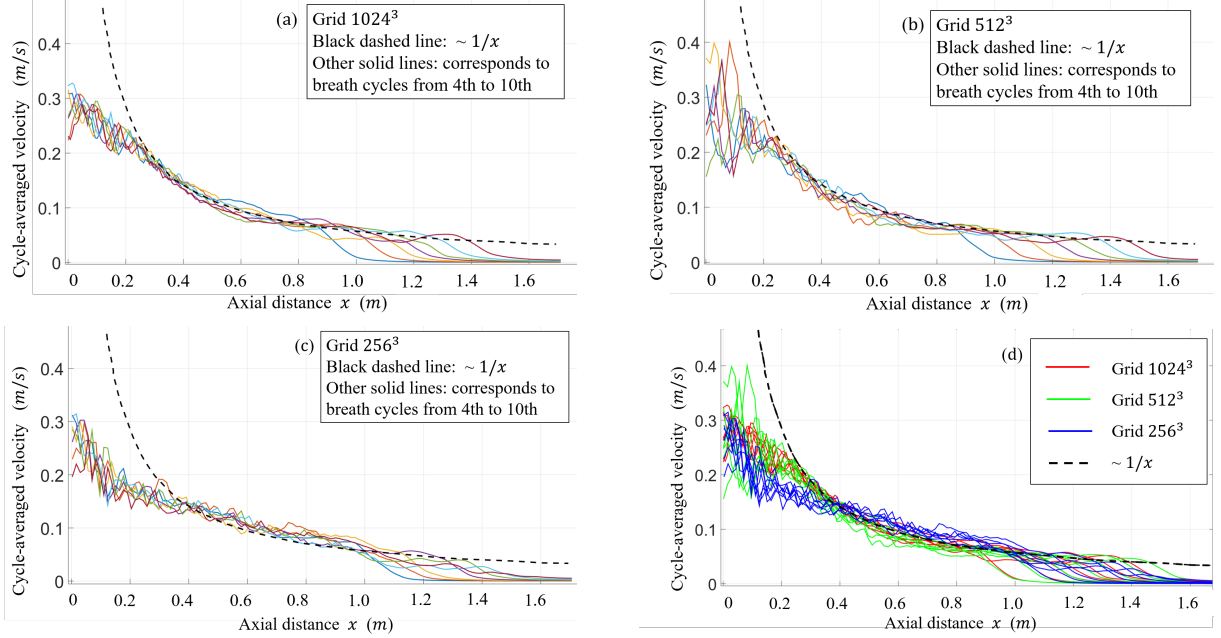


Figure 2: Cycle-averaged centreline velocity versus axial distance (in m) for the grids (a) 1024^3 (b) 512^3 and (c) 256^3 . The black dotted line is the $1/x$ curve of Figure 5D of Abkarian et al. [33]. Other lines show averaged centreline velocity for different cycles (4^{th} to 10^{th}). (d) Comparison of the centreline velocity profiles from the three grids with each other and with the $1/x$ curve.

In figure 3 (a), we plot the passive scalar distribution on the $x - z$ plane at $t = 42.1\text{s}$. Also shown in Fig. 3(a) is a cone of angle $\sim 22^\circ$ which envelops 90% of the instantaneous passive scalar contained in the domain. This cone angle lies in the range of $20^\circ - 28^\circ$ observed by Abkarian et al. [33]. In Figure 3(b), we plot the evolution of the reach of the flow, defined here as the axial distance from the orifice upstream of which $>90\%$ of the scalar concentration exists. The results at all three grid resolutions show the $L \sim t^{1/2}$ behaviour expected for a steady turbulent jet (the red dashed line) for roughly $t > 10\text{s}$, as opposed to the $L \sim t^{1/4}$ behaviour expected for a puff. There is a slight shift of the trajectory for the 256^3 simulations over the time interval of $10 - 35\text{s}$, beyond which there is a good match among the three grid-resolution cases. In the following, we present results on the viral dose and probability of infection over time intervals from 40s to 140s , and therefore the 256^3 grid is expected to give nearly the same results as the two higher-resolution grids. Note that as the turbulent speech flow evolves and grows in space and time, the size of the smallest turbulent eddies increases and therefore a somewhat coarse grid is also expected to give accurate results.

In speech flows, bending of the trajectory due to buoyancy turns out to be negligible due to the small temperature difference between the flow and the ambient. To validate our buoyancy module we have simulated the flow due to a cough, using the same parameters used by Bourouiba et al. [18], where buoyancy effects are not negligible. Figure 4(a) shows the iso-surface of the fluid density for the flow due to a cough, with the dashed circle representing the ‘head’ of the flow. The trajectory of the ‘head’ obtained here matches the experimental observations of Bourouiba et al. [18] well, as shown in Fig. 4(b).

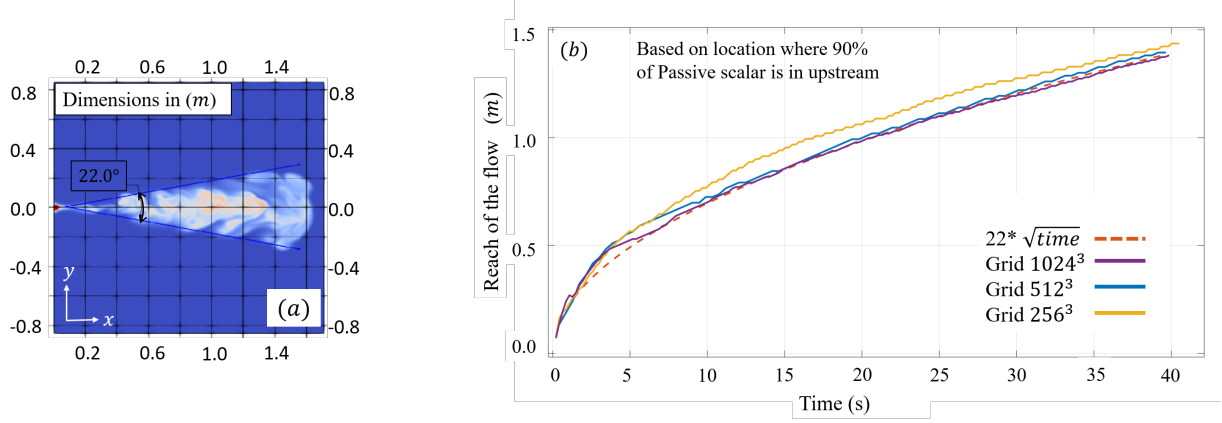


Figure 3: (a) Passive scalar color contours are shown on plane $z = 0$ at a time instance of 42.1 s. The cone of an angle $2\alpha = 22.0^\circ$ includes 90% of the passive scalar. (b) Time variation of the axial extent of the flow, calculated based on 90% of total exhaled passive scalar present upstream of it.

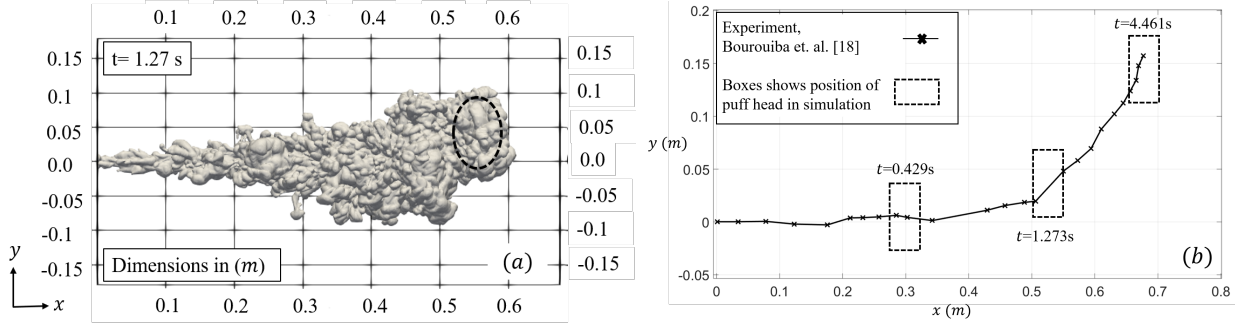


Figure 4: (a) Density difference iso-surface equal to 1% of that of its orifice value (0.00315 g/cm^3) at 1.27 s after flow initiation. The dashed circle representing the 'head' of the flow is selected based on the front edge and shape of this iso-surface. (b) A box spanning axial and vertical extent of the cough-flow head as represented in (a) is overlaid on the trajectory of the flow from Fig. 11 of Bourouiba et. al. [18].

3 Results and Discussion

We return to the case of speech flows for the remainder of this paper, first extending the results for flows due to a single speaker, and then reporting results from a parametric study of two-speaker conversations.

3.1 Single speaker case

The inlet velocity prescribed at the orifice in Section 2 is modified here by extending the duration of a speech 'cycle', as follows. Instead of the 2.8 s + 1.2 s (speech + halt) cycle, we use a 2.8 s + 4.2 s cycle (figure 5) to accommodate speech from the second speaker; the second speaker, when present, speaks between $t = 3.5$ s and $t = 6.3$ s of every cycle (see Section 3.2). The computational domain for the single-speaker case is chosen to be $80d \times 40d \times 40d$ ($\approx 196 \text{ cm} \times 98 \text{ cm} \times 98 \text{ cm}$) with the grid resolution nearly the same as that for the 256^3 domain used earlier. The slightly longer domain size ensures that it is longer than $1.8m$ (to test the $6ft$ rule). The vertical and lateral extents of $40d$ are sufficient due to the small spread angle of the speech flow and the open boundary conditions used on these faces ensure that the flow within the domain is not affected.

3.1.1 Scalar flux and viral exposure

Yang et. al. [34] calculate the infection probability based on the number of virions inhaled by a susceptible listener. However, several studies have found that infections may also be caused by viral contact through other exposed areas like the eyes [39, 40, 41, 42] or the mouth and lips. In order to include these possibilities, we estimate the exposure of a

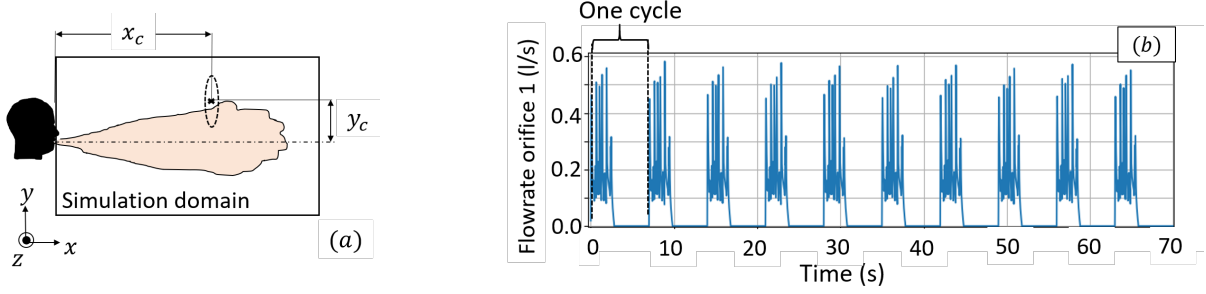


Figure 5: (a) Side view ($z = 0$) of the location of the region of interest (ROI) with respect to the orifice in a single speaker case. x_c and y_c indicate the horizontal (axial) and vertical distances from the orifice 1. (b) Time variation of inlet flow rate through orifice 1 specified for the single speaker simulation.

listener to virus-laden droplets by calculating the flux

$$f(x_c, y_c, t) = \iint C_s u \, dy \, dz, \quad 2\sqrt{(y - y_c)^2 + z^2} < 17.2 \text{ cm} \quad (5)$$

of the scalar C_s through a circular region of interest (ROI) of diameter 17.2 cm, approximately the size of a human face, with its centre point given by $(x_c, y_c, z = 0)$ that can be varied. The ROI is positioned in front of an imaginary listener for determining the viral exposure to the them. Since the deflection of the flow by buoyancy is negligible (as can be seen from figure 12), we note that the y and z directions are equivalent. We therefore need only vary x_c and y_c . The scalar flux is then scaled appropriately to find the number of droplets or dried-up droplet nuclei per unit time; since their sizes are less than $10 \mu\text{m}$ for the speech flow we refer to them as “aerosols”.

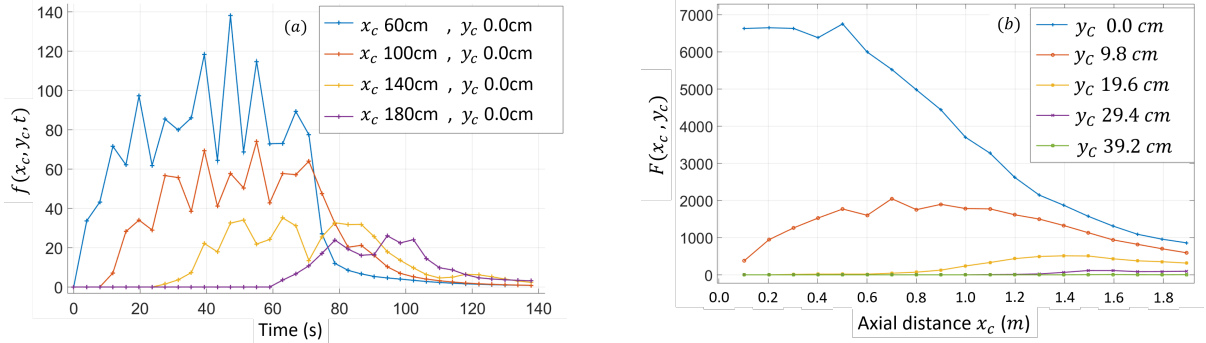


Figure 6: (a) Time variation of passive scalar flux passing across ROI at various axial locations in a single speaker case. The area under these curves represents the values of $F(x_c, y_c)$ plotted in (b). (b) The amount of aerosol exposed to the listener located at x_c and y_c from a single speaker speaking from the left orifice. For $y_c \neq 0$, the value of $F(x_c, y_c)$ is seen to rise with increasing x_c .

In figure 6 (a), we plot the passive scalar flux as a function of time, for different axial locations x_c of the ROI, with $y_c = 0$. The transition of the flow from puff-like behaviour to jet-like behaviour can be seen from the decrease in the oscillations of the scalar flux for larger x_c . The total aerosol exposure to the imaginary listener is given by the time integral of the scalar flux through the ROI,

$$F(x_c, y_c) = \int f(x_c, y_c, t) dt, \quad (6)$$

and is plotted in figure 6(b) as a function of the axial location x_c for five different vertical locations y_c . The time integration is performed over 140s, which is the duration up to which the simulation is carried out (figure 6a). Note that this duration is twice the total speech duration of 70s and represents the time up to which the ROI continues to receive scalar flux. We note from figure 6(b) that the total exposure is nearly constant for $x_c < 50\text{cm}$, because the area of the ROI is larger than the cross-section of the jet till the corresponding axial location. Once the jet cross-section area exceeds the area of the ROI, the total exposure starts decreasing. When listener and speaker are not aligned face to face ($y_c \neq 0$), F increases with x_c for $x_c < y_c / \tan \alpha$, before decaying at large x_c ; here α is the half angle of the speech jet.

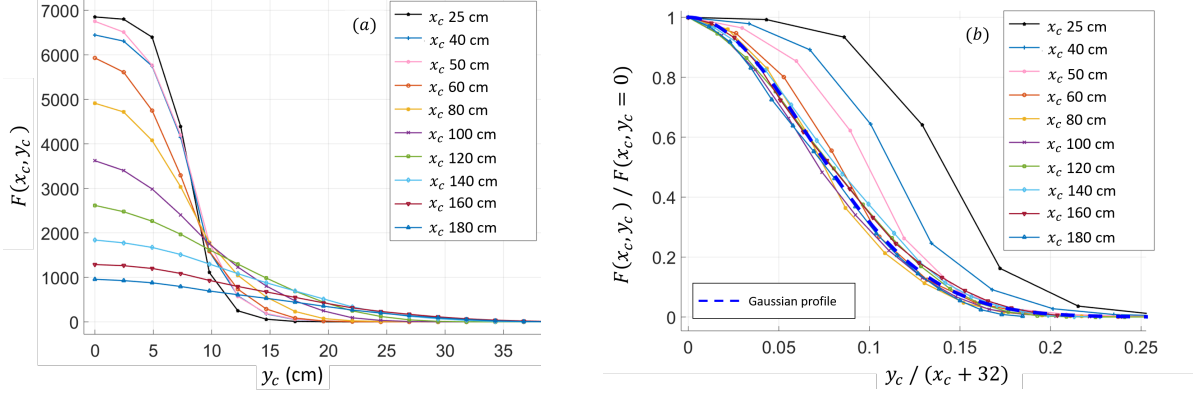


Figure 7: (a) Variation of $F(x_c, y_c)$ with y_c for different axial distances. (b) Scaled distribution of $F(x_c, y_c)$ and its comparison with a Gaussian curve typical of steady-jet profiles. x_c is shifted by a virtual origin of 32cm upstream of orifice.

In figure 7(a), the variation of total aerosol exposure is plotted against the vertical distances y_c , for different axial distances x_c . As the value of x_c increases, the peak value of $F(x_c, y_c)$ at a given x_c decreases and its vertical spread y_c increases. This shows the spreading of puff/jet flow along the axial distance. For $y_c < 10$ cm, $F(x_c, y_c)$ decreases with increasing x_c whereas this trend is reversed for $y_c > 15$ cm. The scaled profiles of $F(x_c, y_c)$ are plotted in Fig. 7 (b). The figure shows that for $x_c = 25$ cm, 40cm, and 50cm, the profiles of F exhibit a bell-shaped behaviour and approach towards a Gaussian distribution (shown by a dashed curve) with increasing x_c . For $x_c \geq 50$ cm, the curves collapse well onto the Gaussian curve. Note that the Gaussian distribution for the scalar flux profiles (and the associated $1/x$ variation of the centreline flux value) is typical of a “self-similar” jet. The bell-shaped profiles in figure 7(b) for $25\text{cm} < x_c < 50\text{cm}$ suggest that flow is in a transition state between a puff and a steady jet. Referring to figure 6(b), the $1/x$ variation of the centreline scalar concentration starts from $x \approx 0.45$, which is commonly used as an indicator for the start of the self-similar regime. In the following we use this location as the beginning of steady, self-similar speech flow.

3.1.2 Top-hat and Gaussian jet profiles

Based on the observed self-similarity of the steady speech flow, Abkarian et al. [33] and Yang et al. [34] have used the steady-jet area averaged scalar concentration ($\phi(x)$) to estimate number of virions transported per unit air volume ($N(\phi) = c_v \phi(x) = c_v \phi_o A / (x \tan \alpha)$), where c_v and ϕ_o are, respectively, the number of virions per unit volume of saliva and volume fraction of saliva in exhaled air, and A is the orifice area. We note, however, that Yang et al.’s formulation does not include radial variations of the scalar concentration; it is thus to be interpreted as a “top-hat” profile with a top-hat radius of $r_H = x \tan \alpha$ chosen based on cone half-angle (α) covering 90% of the scalar inside it. For $r > r_H$, the scalar flux is approximated as zero. Here and in the following, we use a subscript ‘H’ to denote quantities obtained using a top-hat profile.

In classical steady (and self-similar) jets, on the contrary, we know that the velocity and passive scalar concentration radial profiles are Gaussian, with characteristic widths b_{ue} and b_{Ce} respectively (figure 7b). Jet widths are overestimated if a top-hat profile is used, with $r_H(x) = 1.516b_{Ce}(x) = 1.819b_{ue}(x)$ for the definition of r_H used by Yang et al. [34]. As a result of this, the jet velocity and the passive scalar concentration used by them are *underestimated*, with $v_H(x) = 0.39U_c(x)$ and $\phi_H(x) = 0.462C_{sc}$, where U_c and C_{sc} are the (Gaussian) centreline velocity and scalar concentration. The various radii are shown on a representative Gaussian profile in figure 8(a), and the details of the calculation are given in Appendix I. The (Gaussian) centreline and the top-hat passive scalar concentration are plotted against axial distance in figure 8(b). As mentioned earlier, the self-similar $1/x$ behaviour for the speech jet in the present simulations is evident for $x > 45$ cm.

From the above calculation it appears that the use of the top-hat scalar concentration ϕ_H in [34] could lead to an underestimation of the number of virions inhaled by the listener, although it is a good starting point. We provide below a better estimate of the average passive scalar concentration, ϕ_{new} , using a Gaussian profile.

$$\phi_{new} = \left(\frac{b_{Ce}}{6.2}\right)^2 [1 - \exp(-1 * (\frac{6.2}{b_{Ce}})^2)] C_{sc}. \quad (7)$$

In equation (7) the Gaussian profile for the time-mean scalar concentration is averaged over a circular area of radius 6.2cm. This is a typical radius of the hemispherical region centred at the mouth from which air is drawn (about 0.5

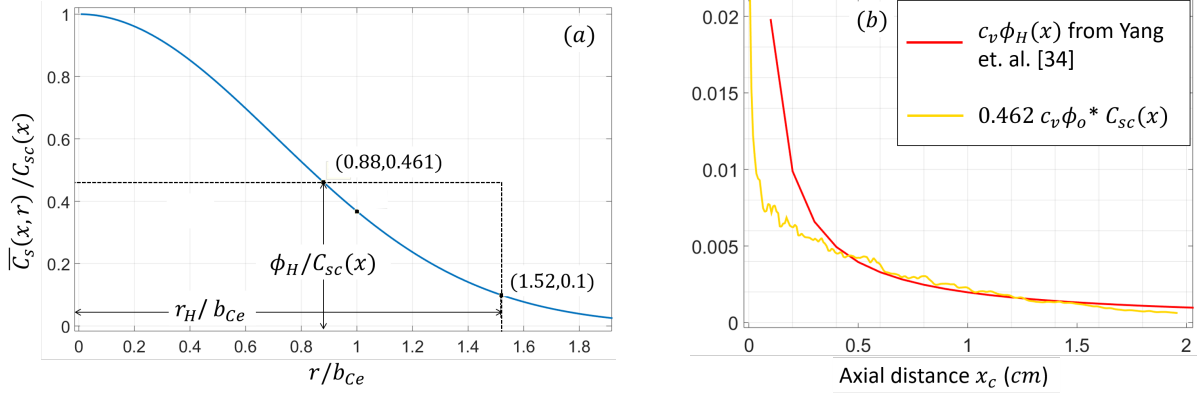


Figure 8: (a) Gaussian distribution for the time-mean passive scalar concentration \overline{C}_s , relating the characteristic definitions of radii (b_{Ce} , r_H) and passive scalars (C_{sc} , ϕ_H) used in this study and that of Yang et. al. [34]. ϕ_H [34] is shown by the dashed top-hat profile over a radius of r_H/b_{Ce} with a height equal to $0.461C_{sc}$. This illustrates the likely underestimation of number of virions inhaled from the region near the jet axis for $r/b_{Ce} < 0.88$. (b) The top-hat decay of the passive scalar compared with the decay for a Gaussian profile, with a pre-factor of 0.462.

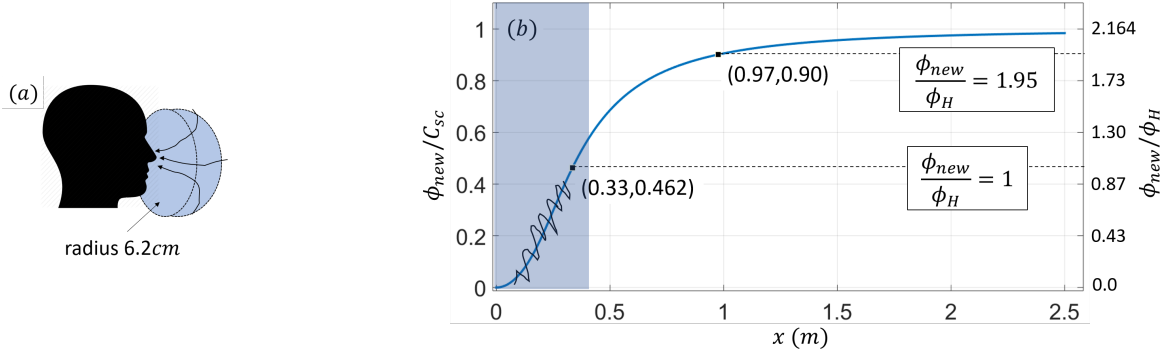


Figure 9: (a) Schematic of the hemispherical region around the mouth of a person affected during the inhalation process. (b) The axial variation of ϕ_{new} (equation 7) and its comparison with ϕ_H .

litres) during the inhalation process (see Fig. 9 (a)) [33, 43]. This results in the new measure of virion exposure ϕ_{new} ; see Appendix II for details. Figure 9 (b) shows that $\phi_{new} > \phi_H$ for $x > 45\text{cm}$; the region up to this axial location is shown shaded as the Gaussian profile does not apply in this region. Figure 9(b) also shows that for $x > 1\text{m}$, $\phi_H(x) \approx 0.5\phi_{new}(x)$; the use of the top-hat profile thus underestimates infection by direct inhalation of viruses by about 50%, supporting our expectation mentioned earlier.

3.1.3 Viral exposure and infection probability

The axial variation of the number of virions $N(\phi_H(x))$ and $N(\phi_{new}(x))$ for the ROI located at x_c and $y_c = 0$ (i.e., at the place of an imaginary listener) are plotted in figure 10(a). The corresponding infection probabilities, $p(N) = 1 - e^{-N/N_{inf}}$, where $N_{inf} \approx 100$ is the characteristic number of virions necessary for infection [14, 35], are plotted in Fig. 10(b). The blue curve is figure 10(a) represents the total exposure to the listener over 140s. This corresponds to the maximum number of virions that a listener can be exposed to, given as

$$N_s = c_v \phi_o F(x_c, y_c). \quad (8)$$

Figure 10(a) shows that N_s is significantly larger than $N(\phi_H)$ and $N(\phi_{new})$ for all x . Contrary to the steep decline near the orifice of $N(\phi_H)$, N_s is nearly constant for $x \lesssim 0.5\text{m}$ (see also Fig. 6(b)). Note that this is the region where the self-similarity of the speech flow does not hold, and therefore the steep decay shown by $N(\phi_H)$ is expected to be unrealistic.

Typically the number of virions inhaled is considered for calculating the probability of infection. However, this is likely to underestimate infection probabilities, as ingestion of virions through the eyes and mouth opening should also be

included. We assume that viral exposure through the eyes and mouth is a fraction (κ) of N_s , where $\kappa = A_{em}/A(ROI)$; here A_{em} is the total area of eyes and mouth and $A(ROI)$ is the area of the ROI (i.e. the projected face area). The total number of virions that a listener is exposed to is, therefore,

$$N_{is} = N(\phi_{new}) + \kappa \cdot N_s. \quad (9)$$

Reasonable estimates for the areas of the eyes (radius $\approx 24mm$) and of the mouth and lips ($\approx 15.55cm^2$), suggest that these amount to about 10.6% of the area of the face. N_{is} and its corresponding infection probability, for two values of $\kappa = 10.6\%$ and 20% are plotted in Fig. 10. (The higher value of 20% is chosen to provide a more conservative estimate.) As can be seen from figure 10(b), the probability of infection $p(N_{is})$ is 2 to 3 times higher than that obtained based on $N(\phi_H)$, over the separation distances ranging from $2ft$ to $6ft$.

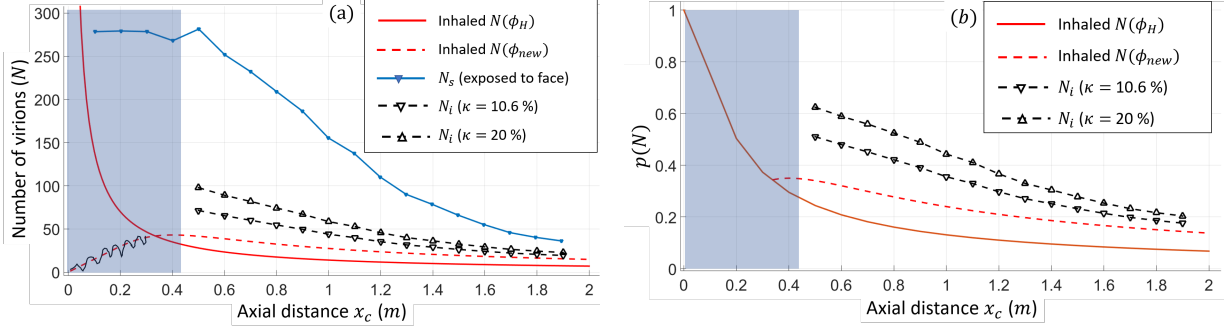


Figure 10: (a) Number of virions N_s , $N(\phi_H)$ and $N(\phi_{new})$ (see text for definitions) the listener inhales or otherwise comes into contact with (b) Corresponding infection probabilities for a total simulation time of 140s (i.e., twice the speech time).

3.2 Two speaker conversation

Thus far, similar to previous studies [34], the ‘listener’ has been entirely passive. We now look at cases where two persons are in conversation, and the flows thus generated interact. The geometry and flow cycles are modified from Sec. 3.1 as follows. The orifice for speaker 1 is located at $(0, 0.5 * y_s, 0)$ and that for speaker 2 at $(L_s + \Delta, -0.5 * y_s, 0)$, as shown schematically in Fig. 11(a). The two speakers are thus separated in x by $L_s + \Delta$, and in y by y_s . The inlet flow rates at the two orifices are as shown in Fig. 11(b). In order to avoid wall effects, the ROI for speaker 2 (for whom the risk of infection will be determined) is located at $(L_s, -0.5 * y_s, 0)$, that is at a distance Δ from the right wall. We report below the results from systematically varying L_s and y_s .

Separate passive scalars C_{s1} and C_{s2} are used for the two speakers, each governed by equation 4. Owing to the presence of a second speaker, the boundaries at $x = 0$ and $x = L_s + \Delta$ are taken to be free-slip walls instead of outflow boundaries. The four lateral faces remain open boundaries as before. We find that the flows generated by an either speaker are comparable to the flow generated by an undisturbed single speaker in Sec. 3.1.

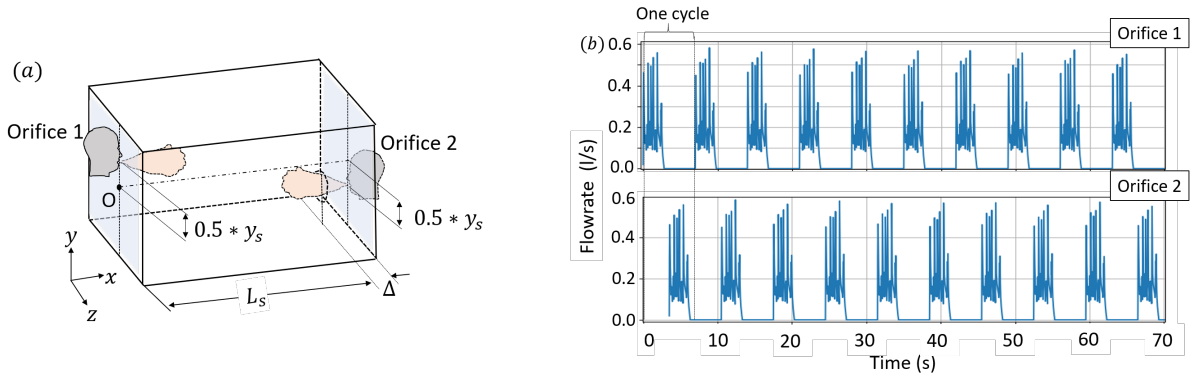


Figure 11: (a) Schematic of the computation domain for two speakers and (b) inlet flow rates at the two orifices.

The flux f of the scalar C_{s1} at the ROI of speaker 2, for three different values of $L_s \in 60\text{cm}, 120\text{cm}, 180\text{cm}$ are reported in the following plots. For each value of L_s , simulations were carried out for seven different values of $y_s = 0d, 2d, 4d, 6d, 8d, 12d$ and $16d$.

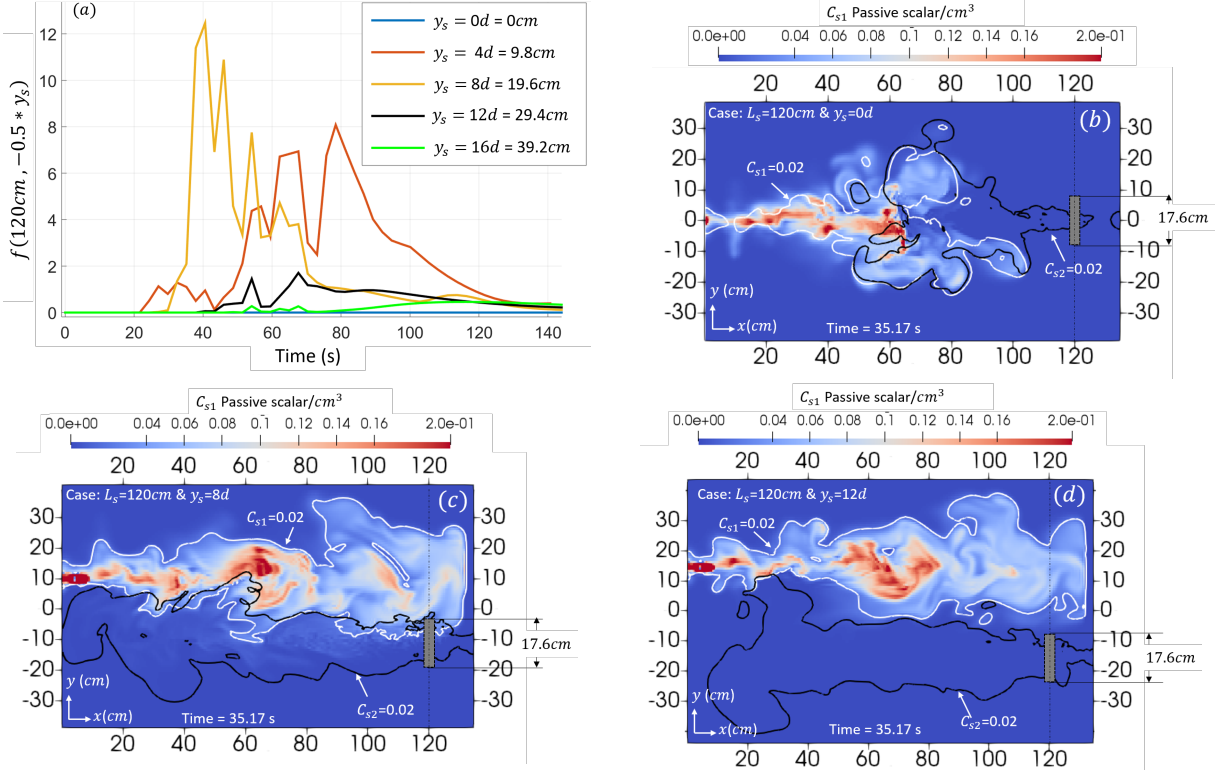


Figure 12: (a) Passive scalar flux across the circular region centered at $L_s = 120\text{cm}$ and y -shift at $-0.5*y_s$; y_s is mentioned in terms of d . (b-d) passive scalar contours for $L_s = 120\text{cm}$ at $t = 35.17\text{ s}$ for y_s of $0d, 8d$ and $12d$, respectively. A demarcation of 2% of scalar value at orifice is shown to define the boundary of both the jets. The colour contours are shown only for C_{s1} . A side view of ROI in front of the second speaker is represented by a grey box.

Figure 12 (a) shows $f(C_{s1}; L_s, y_s, t)$ for $L_s = 120\text{cm}$ as y_s is varied. For larger L_s , the peaks of $f(L_s, y_s, t)$ occur for larger t , as may be expected, and the simulations are run until $f(C_{s1}; L_s, y_s, t)$ has reduced sufficiently. Figure 12(a) also shows that $f(C_{s1}; L_s, y_s, t)$ varies non-monotonically with y_s , with the highest peak occurring at an intermediate value of $y_s = 19.6\text{cm}$. A contour plot of the instantaneous passive scalar concentration C_{s1} and the contours $C_{s(1,2)} = 0.02$ are shown in Figs. 12(b-d) for $y_s = 0d, 8d, 12d$ respectively. In figure 12(b) ($y_s = 0d$), the jets issuing out of the two orifices collide and ‘cancel’ each other out, and form a cloud in the middle. As a result, the flux of C_{s1} at speaker 2 is much smaller than what it would be if speaker 2 were passive. For $y_s = 8d$ the interference between the two jets is significantly reduced and therefore the aerosols from speaker 1 find it easier to reach the ROI positioned in front of speaker 2 (figure 12b). For $y_s = 12d$, the interference between the left and right jets is minimal but the left jet does not contribute much to the ROI scalar flux, due to the large vertical separation between the jets. The competing effects of the jet interference and vertical separation lead to the observed maximum in the scalar flux for intermediate y_s (figure 12a).

3.2.1 Viral exposure and infection probability

As in Sec. 3.1.3, the maximum exposure of speaker 2 to the virions exhaled by speaker 1 is given by

$$N_c(C_{s1}; L_s, -0.5 * y_s) = c_v \phi_o F(C_{s1}; L_s, -0.5 * y_s). \quad (10)$$

N_c is plotted as a function of L_s and y_s in figure 13(a) and, as expected, decreases with increasing L_s . Figure 13 also shows, however, that N_c peaks for intermediate y_s . This is due to the cancellation of the oppositely oriented jets for small y_s , as described in figs. 12. The curves for different L_s are normalised by their maximal values and these normalised curves are plotted against y_s/L_s in figure 13(b). We find that the maximum in N_c occurs at y_s/L_s of $\approx 0.1 - 0.2$ which can be a useful result in determining y_s that provides largest exposure to virus for a given L_s .

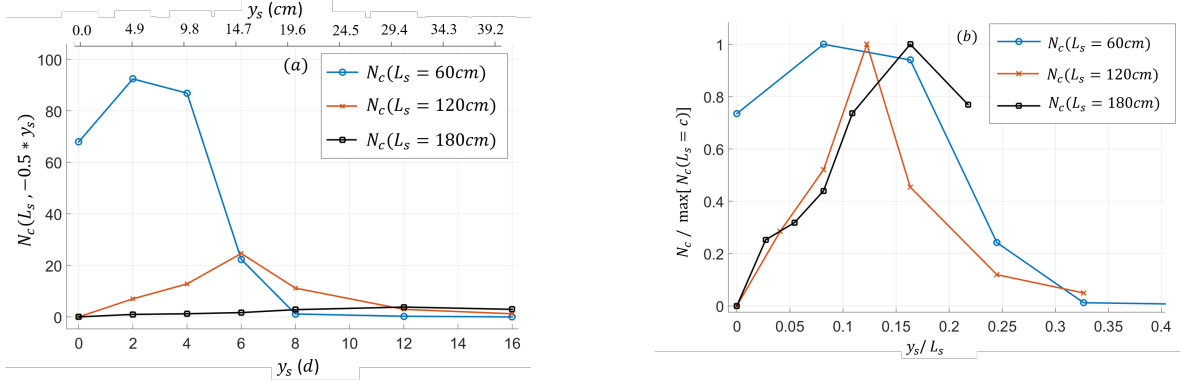


Figure 13: (a) Total viral exposure to the face of speaker 2 (N_c) for different values of L_s and y_s . (b) The value of N_c in (a) is normalised with its maximum value for corresponding L_s .

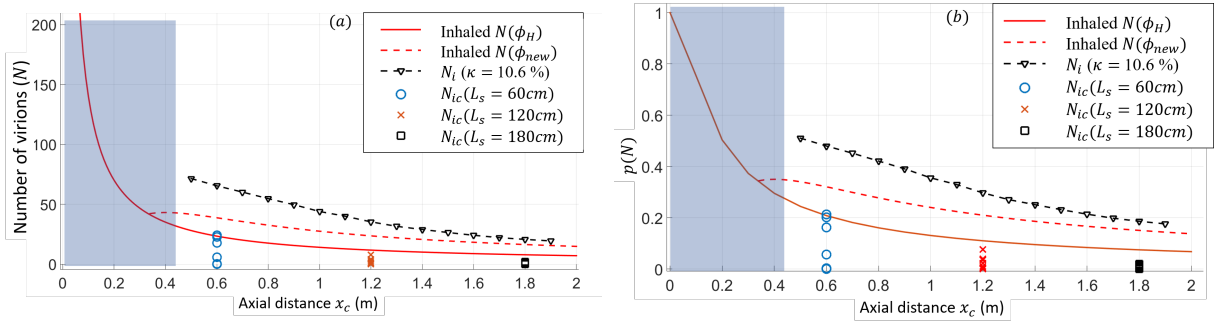


Figure 14: (a) The number of Virions ingestion by speaker 2 for two speaker conversation (N_{ic}), overlaid on the curves from figure 10. (b) the probability of infection to speaker 2 as a function of axial distance.

To calculate the viral exposure and corresponding infection probabilities, we assume that

$$\frac{N_{ic}}{N_c} = \frac{N_{is}}{N_s}, \quad (11)$$

where N_{ic} represents the number of virions ingested by speaker 2 through inhalation and thorough exposure to eyes and mouth. N_{ic} is defined analogously to N_{is} , both fractions are functions of κ , and the fraction on the right is obtained from Eq. (9).

In Fig. 14, the viral exposure and infection probabilities for $\kappa = 10.6\%$ are overlaid on the curves from Fig. 10 obtained for a passive listener. The symbols corresponding to seven different values of y_s are placed at $x = L_s$. We see that the infection probability varies significantly as y_s is varied for fixed L_s . We note that due to the presence of a jet in the opposite direction, $N_{ic} \leq N_{is}$ (and $p(N_{ic}) < p(N_{is})$), implying that people in conversation are less likely to get infected than passive listeners.

4 Discussion

The results obtained here could provide guidance on the separation distance for a safe interaction among people engaged in a short conversation (up to about a minute or two). This situation arises routinely in day-to-day life, especially in shopping malls or stores, wherein the over-the-counter conversations take place for a short duration. The separation distances between two people can be 2ft or smaller. Furthermore, if the persons involved are asymptomatic they tend not to wear a mask or lower the already worn mask for ease of conversation. The present simulations show that the probability of infection is largest when the height difference between the conversing people separated by 2ft is about 10cm. The risk of infection decreases on either side of this height difference; in particular people of comparable heights and having height differences of more than 20cm have a less risk of infection during a short conversation. These are useful inputs. More importantly, the results obtained here for vertical separation distance are also equally valid for lateral separation distance (since the effect of buoyancy is shown to be negligible). It is therefore possible to come up

with universal guidelines applicable for conversing people with any height difference. For a separation distance of 2ft between two people, if they ensure that there is a lateral separation of 20cm or more, they are at a significantly lower risk of infection. This can be achieved by simply turning their faces away from each other (instead of physically moving 20cm laterally; figure 15a) by an angle (equal to $\tan^{-1}(10/60) = 10^\circ$) so that the jet created from one person's mouth is not directed towards the other person's face (figure 15b). This will enable the conversation to be safe while still enabling eye contact.

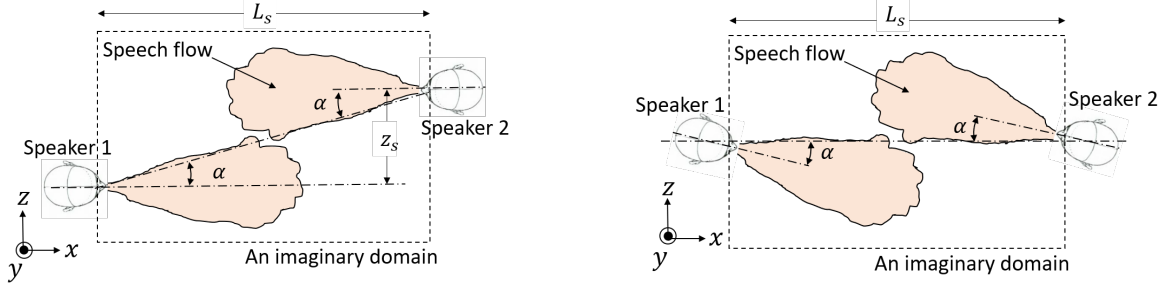


Figure 15: (a) Schematic of two people separated laterally by a distance z_s such that the risk of infection is minimized. (b) Schematic of two people conversing with their heads turned away from each other by a small angle to achieve the same effect as in (a). For 2ft axial separation, a tilt angle of 10° is sufficient.

Moreover the present simulations can provide useful inputs to epidemiological models to improve their prediction accuracy. In this connection, Chaudhury et al. [23] have presented a framework for determining the infection rates for different expiratory events such as coughing, sneezing, breathing, talking etc and incorporating them in the SEIRD (susceptible-exposed-infected-recovered-deceased) model. They have highlighted the need for an accurate data on viral exposure based on fluid dynamical simulation of these expiratory events. Since the present simulations provide a spatio-temporal distribution of scalar field, the quantities needed as inputs to the model for determining the infection risk due to speaking can be easily calculated. We have found that the probability of infection for a conversation depends upon the distance between the two people. It may be possible to consider a scenario wherein, a certain percentage of the population of an area or a city (say 30%) follow the guideline of 6ft separation during a conversation, a certain percentage (say 30%) maintain a distance of 4ft, while the remaining fraction (40%) flout the guidelines and maintain only 2ft distance. We could then use the probability of infection for each case to come up with a composite value for the resultant probability that can serve as an input to the model. We could also add another level of complexity: we could have a distribution of the short conversation times and use them as weighing functions for the corresponding probabilities of infection to come up with a final number. As can be seen, the present DNS study is capable of providing information for any level of complexity required for improving the existing epidemiological models.

The limitations of the present simulation results should also be noted. Overestimation of infection probability due to absence of external influence on flow and its underestimation due to overlooking of fact that inhalation is a localised process, should be taken into account. Furthermore, other parameters like c_v could be an order of magnitude larger than the values used here [44]; the number of droplets exhaled is also a function of the loudness of speech [16]. Given the vast ranges of these parameters, mask mandates are crucial in curbing disease transmission [45].

5 Concluding remarks

We have performed direct numerical simulations of the transmission of virus-laden aerosols by the flows generated in human speech during short conversations. The main results of the study are listed below.

1. We have computed the total exposure that a listener can get due to the speech flow from the speaker (for one speaker and conversation). This has enabled us to calculate the infection dose not only through inhalation but also through the mouth and eyes. The probability of infection is calculated based on the total number of ingested virion and is found to be higher by a factor of 2-3 compared to the estimate given by Yang et al. [34].
2. For two people speaking, for a given axial separation distance, the viral exposure to the listener is much smaller than that for the single speaker case and therefore the single speaker case gives a gross over-estimation of the risk of infection. This is because the jets coming out of two speaker mouths interact and slow down the advection of the virions to the other person.
3. We find an interesting result that the risk of infection is maximum for a certain vertical separation, which is proportional to axial separation, with the proportionality constant between 0.1 and 0.2. This result also applies

for the lateral separation and can enable devising public health guidelines of minimum lateral separation to reduce the risk of infection during a short conversation.

Several recent attempts to study viral transmission rely on models of the flow (e.g. [23]), and the results in these studies are only as reliable as these flow models. Well-resolved numerical simulations such as presented here could help improve the flow models in such studies. Lastly, the sensitive dependence of viral exposure on the several parameters studied here also provides some insight into why the guidelines issued by various authorities have proved to be insufficient in curbing the spread of SARS-CoV-2.

Acknowledgments

The simulations were carried out at the Supercomputer Education and Research Centre at IISc, Bangalore. SR gratefully acknowledges support through the Swedish Research Council grant no. 638-2013-9243. SSD acknowledges support from IISc Bangalore in the form of a start-up grant.

Appendix I

In this appendix, we have compare the top-hat profiles in Yang et. al. [34] and Gaussian steady jet profile characteristics like centerline parameters and exponential ($1/e$) width. Exponential width is radial distance from the jet axis where value of quantity drops down to $1/e$ times of its centerline quantity. The steady state jet parameters like time-averaged axial velocity and passive scalar profile are defined as:

$$\overline{u_x}(x, r) = U_c \exp(-(r/b_{ue})^2), \quad (12)$$

$$\overline{C_s}(x, r) = C_{sc} \exp(-(r/b_{Ce})^2). \quad (13)$$

Here, b_{ue} and b_{Ce} are exponential widths of axial velocity and passive scalar profiles. Yang et. al. [34] define the jet radius $r_H = x \tan \alpha$, based on the cone of half angle α which covers 90% of total passive scalar in it. The amount of passive scalar in an area of radius r from its axis:

$$F = \int_0^r \overline{C_s}(x, r) 2\pi r dr = C_{sc} \pi b_{Ce}^2 [1 - \exp(-(\frac{r}{b_{Ce}})^2)]. \quad (14)$$

Total amount of passive scalar could be found from integration over whole planner area,

$$F_{total} = C_{sc} \pi b_{Ce}^2 \text{ at } r = \infty. \quad (15)$$

To find r_H , substitute $F = 0.9F_{total}$ in equation 14, leading to

$$0.9C_{sc} \pi b_{Ce}^2 = C_{sc} \pi b_{PSe}^2 [1 - \exp(-(\frac{r_H}{b_{Ce}})^2)]. \quad (16)$$

The equation 16 gives us the relation between r_H and b_{Ce} as

$$r_H = 1.516b_{Ce} = 1.819b_{ue}. \quad (17)$$

Literature [46] provides a relationship between axial velocity width and passive scalar width as $b_{Ce} = 1.21b_{ue}$. Using the above relation and the property that momentum flux remains constant along the steady jet's axis, we could compare the top-hat velocity with centerline quantity. The momentum flux is:

$$v_H^2(x)A(x) = \int_0^\infty \overline{u_x}^2(x, r) 2\pi r dr, \quad (18)$$

$$v_H^2(x) \pi [1.819]^2 b_{ue}^2 = 0.5 * U_c^2 \pi b_{ue}^2, \quad (19)$$

$$v_H(x) = 0.39U_c. \quad (20)$$

This gives a relation between two forms of velocity parameters. Further for deciding the passive scalar relation, we could use the property of constant passive scalar flux relation with respect to the axial distance as:

$$\phi_H(x)v_H(x)A(x) = \int_0^\infty \overline{C_s}(x, r)\overline{u_x}(x, r) 2\pi r dr, \quad (21)$$

$$\phi_H(x)v_H(x)\pi[1.819]^2b_{ue}^2 = C_{sc}U_c\pi\frac{b_{ue}^2 \cdot b_{Ce}^2}{b_{ue}^2 + b_{Ce}^2}, \quad (22)$$

$$\phi(x) = 0.462C_{sc}. \quad (23)$$

Hence, the top-hat passive scalar profile used in Yang et.al. [34] have a much lower value than centerline passive scalar value in a Gaussian profile.

Appendix II

The person draws air from circular region of radii 6.2cm having its center coinciding with the jet axis. The average passive scalar value near jet axis based on this circular region is computed as:

$$\int_0^{6.2\text{cm}} \overline{C_s}(x, r)2\pi r dr = \phi_{new}\pi 6.2^2 = C_{sc}(x)\pi b_{Ce}^2[1 - \exp(-(\frac{6.2}{b_{Ce}})^2)]. \quad (24)$$

Further, to convert b_{ue} in terms of axial distance, the relation $b_{ue} = 0.114(x - x_o)$ mentioned in Singhal et. al. [38] is used.

References

- [1] Sima Asadi, Nicole Bouvier, Anthony S. Wexler, and William D. Ristenpart. The coronavirus pandemic and aerosols: Does covid-19 transmit via expiratory particles? *Aerosol Science and Technology*, 54(6):635–638, 2020. PMID: 32308568.
- [2] Lidia Morawska and Junji Cao. Airborne transmission of SARS-CoV-2: The world should face the reality. *Environment International*, 139(April):105730, 2020.
- [3] Lydia Bourouiba. The fluid dynamics of disease transmission. *Annual Review of Fluid Mechanics*, 53(1):473–508, 2021.
- [4] W. F. WELLS. Droplets and Droplets nuclei. *American Journal of Epidemiology*, 20(3):611–618, 1934.
- [5] Kimberly A. Prather, Chia C. Wang, and Robert T. Schooley. Reducing transmission of SARS-CoV-2. *Science*, 368(6498):1422–1424, 2020.
- [6] J. P. Duguid. The size and the duration of air-carriage of respiratory droplets and droplet-nuclei. *Journal of Hygiene*, 44(6):471–479, 1946.
- [7] G. R. Johnson, L. Morawska, Z. D. Ristovski, M. Hargreaves, K. Mengersen, C. Y.H. Chao, M. P. Wan, Y. Li, X. Xie, D. Katoshevski, and S. Corbett. Modality of human expired aerosol size distributions. *Journal of Aerosol Science*, 42(12):839–851, 2011.
- [8] Saptarshi Basu, Prasenjit Kabi, Swetaprovo Chaudhuri, and Abhishek Saha. Insights on drying and precipitation dynamics of respiratory droplets from the perspective of covid-19. *Physics of Fluids*, 32(12):123317, 2020.
- [9] Rajneesh Bhardwaj and Amit Agrawal. Likelihood of survival of coronavirus in a respiratory droplet deposited on a solid surface. *Physics of Fluids*, 32(6):061704, 2020.
- [10] Michael Schuit, Shanna Ratnesar-Shumate, Jason Yolitz, Gregory Williams, Wade Weaver, Brian Green, David Miller, Melissa Krause, Katie Beck, Stewart Wood, et al. Airborne SARS-CoV-2 is rapidly inactivated by simulated sunlight. *The Journal of infectious diseases*, 222(4):564–571, 2020.
- [11] U.S. Department of Homeland Security. Estimated airborne decay of SARS-CoV-2. *Technical Report*, 2020.
- [12] Linsey C Marr, Julian W Tang, Jennifer Van Mullekom, and Seema S Lakdawala. Mechanistic insights into the effect of humidity on airborne influenza virus survival, transmission and incidence. *Journal of the Royal Society Interface*, 16(150):20180298, 2019.
- [13] Lydia Bourouiba. Turbulent Gas Clouds and Respiratory Pathogen Emissions: Potential Implications for Reducing Transmission of COVID-19. *JAMA*, 323(18):1837–1838, 05 2020.
- [14] Saikat Basu. Computational characterization of inhaled droplet transport to the nasopharynx. *Scientific Reports*, (6652), 2021.
- [15] Scott H. Smith, G. Aernout Somsen, Cees van Rijn, Stefan Kooij, Lia van der Hoek, Reinout A. Bem, and Daniel Bonn. Probability of aerosol transmission of SARS-CoV-2. *medRxiv*, 2020.

- [16] Sima Asadi, Anthony S. Wexler, Christopher D. Cappa, Santiago Barreda, Nicole M. Bouvier, and William D. Ristenpart. Aerosol emission and superemission during human speech increase with voice loudness. *Scientific Reports*, (1):1–10, 2019.
- [17] Jitendra K Gupta, C-H Lin, and Q Chen. Flow dynamics and characterization of a cough. *Indoor air*, 19(6):517–525, 2009.
- [18] Lydia Bourouiba, Eline Dehandschoewercker, and John W. M. Bush. Violent expiratory events: on coughing and sneezing. *Journal of Fluid Mechanics*, 745:537–563, 2014.
- [19] Jianjian Wei and Yuguo Li. Human cough as a two-stage jet and its role in particle transport. *PloS one*, 12(1):e0169235, 2017.
- [20] Raymond P. Clark and Mervyn L. de Calcina-Goff. Some aspects of the airborne transmission of infection. *Journal of the Royal Society Interface*, 6(SUPPL. 6), 2009.
- [21] Julian W. Tang, Thomas J. Liebner, Brent A. Craven, and Gary S. Settles. A schlieren optical study of the human cough with and without wearing masks for aerosol infection control. *Journal of The Royal Society Interface*, 6(suppl_6):S727–S736, 2009.
- [22] Peter V. Nielsen, Inés Olmedo, Manuel Ruiz de Adana, Piotr Grzelecki, and Rasmus L. Jensen. Airborne cross-infection risk between two people standing in surroundings with a vertical temperature gradient. *HVAC and R Research*, 18(4):552–561, 2012.
- [23] Swetaprovo Chaudhuri, Saptarshi Basu, and Abhishek Saha. Analyzing the dominant SARS-CoV-2 transmission routes toward an ab initio disease spread model. *Physics of Fluids*, 32(12):123306, 2020.
- [24] Talib Dbouk and Dimitris Drikakis. Fluid dynamics and epidemiology: Seasonality and transmission dynamics. *Physics of Fluids*, 33(2):021901, 2021.
- [25] H. Qian and Y. Li. Removal of exhaled particles by ventilation and deposition in a multibed airborne infection isolation room. *Indoor Air*, 20(4):284–297, 2010.
- [26] L. Liu, Y. Li, P. V. Nielsen, J. Wei, and R. L. Jensen. Short-range airborne transmission of expiratory droplets between two people. *Indoor Air*, 27(2):452–462, 2017.
- [27] Talib Dbouk and Dimitris Drikakis. On coughing and airborne droplet transmission to humans. *Physics of Fluids*, 32(5):053310, 2020.
- [28] Siyao Shao, Dezhi Zhou, Ruichen He, Jiaqi Li, Shufan Zou, Kevin Mallery, Santosh Kumar, Suo Yang, and Jiarong Hong. Risk assessment of airborne transmission of COVID-19 by asymptomatic individuals under different practical settings. *Journal of Aerosol Science*, 151(August 2020):105661, 2021.
- [29] Kai Leong Chong, Chong Shen Ng, Naoki Hori, Rui Yang, Roberto Verzicco, and Detlef Lohse. Extended lifetime of respiratory droplets in a turbulent vapor puff and its implications on airborne disease transmission. *Phys. Rev. Lett.*, 126:034502, Jan 2021.
- [30] M. E. Rosti, M. Cavaola, S. Olivieri, A. Seminara, and A. Mazzino. Turbulence role in the fate of virus-containing droplets in violent expiratory events. *Phys. Rev. Research*, 3:013091, Jan 2021.
- [31] Alexandre Fabregat, Ferran Gisbert, Anton Vernet, Som Dutta, Ketan Mittal, and Jordi Pallarès. Direct numerical simulation of the turbulent flow generated during a violent expiratory event. *Physics of Fluids*, 33(3):035122, 2021.
- [32] Antoine Giovanni, Thomas Radulesco, Gilles Bouchet, Alexia Mattei, Joana Révis, Estelle Bogdanski, and Justin Michel. Transmission of droplet-conveyed infectious agents such as SARS-CoV-2 by speech and vocal exercises during speech therapy: preliminary experiment concerning airflow velocity. *European Archives of Otorhinolaryngology*, (0123456789), 2020.
- [33] Manouk Abkarian, Simon Mendez, Nan Xue, Fan Yang, and Howard A. Stone. Speech can produce jet-like transport relevant to asymptomatic spreading of virus. *Proceedings of the National Academy of Sciences*, 117(41):25237–25245, 2020.
- [34] Fan Yang, Amir A. Pahlavan, Simon Mendez, Manouk Abkarian, and Howard A. Stone. Towards improved social distancing guidelines: Space and time dependence of virus transmission from speech-driven aerosol transport between two individuals. *Phys. Rev. Fluids*, 5:122501, Dec 2020.
- [35] John M. Kolinski and Tobias M. Schneider. Superspreading events suggest aerosol transmission of SARS-CoV-2 by accumulation in enclosed spaces. *Phys. Rev. E*, 103:033109, Mar 2021.
- [36] Vrishank Raghav, Zu Puayen Tan, and Surya P. Bhatt. Dispersion of speech aerosols in the context of physical distancing recommendations. (5), 2020.

- [37] S. Ravichandran, Eckart Meiburg, and Rama Govindarajan. Mammatus cloud formation by settling and evaporation. *Journal of Fluid Mechanics*, 899:A27, 2020.
- [38] Rohit Singhal, S Ravichandran, Sourabh S Diwan, and Garry L Brown. Reynolds Stress Gradient and Vorticity Fluxes in Axisymmetric Turbulent Jet and Plume. In L. Venkatakrishnan, Sekhar Majumdar, Ganesh Subramanian, G. S. Bhat, Ratul Dasgupta, and Jaywant Arakeri, editors, *Proceedings of 16th Asian Congress of Fluid Mechanics*, Bangalore, 2021. Springer Singapore.
- [39] Minas Theodore Coroneo and Peter John Collignon. Comment SARS-CoV-2 : eye protection might be the missing key. *The Lancet Microbe*, 5247(21):19–20, 2021.
- [40] Xuhui Chen, Huimin Yu, Ting Mei, Bo Chen, Liwen Chen, Shanling Li, Xian Zhang, and Xufang Sun. SARS-CoV-2 on the ocular surface: is it truly a novel transmission route? *British Journal of Ophthalmology*, 2020.
- [41] Hua-Tao Xie, Shi-Yun Jiang, Kang-Kang Xu, Xin Liu, Bing Xu, Lin Wang, and Ming-Chang Zhang. SARS-CoV-2 in the ocular surface of COVID-19 patients. *Eye and Vision*, 7(1):7–9, 2020.
- [42] Chuan Bin Sun, Yue Ye Wang, Geng Hao Liu, and Zhe Liu. Role of the Eye in Transmitting Human Coronavirus: What We Know and What We Do Not Know. *Frontiers in Public Health*, 8(April):1–7, 2020.
- [43] F. R. Haselton and P. G.N. Sperandio. Convective exchange between the nose and the atmosphere. *Journal of Applied Physiology*, 64(6):2575–2581, 1988.
- [44] Roman Wölfel, Victor M. Corman, Wolfgang Guggemos, Michael Seilmaier, Sabine Zange, Marcel A. Müller, Daniela Niemeyer, Terry C. Jones, Patrick Vollmar, Camilla Rothe, Michael Hoelscher, Tobias Bleicker, Sebastian Brünink, Julia Schneider, Rosina Ehmann, Katrin Zwirgmaier, Christian Drosten, and Clemens Wendtner. Virological assessment of hospitalized patients with COVID-2019. *Nature*, 581(7809):465–469, 2020.
- [45] Derek K. Chu, Elie A. Akl, Stephanie Duda, Karla Solo, Sally Yaacoub, Holger J. Schünemann, Amena El-harakeh, Antonio Bognanni, Tamara Lotfi, Mark Loeb, Anisa Hajizadeh, Anna Bak, Ariel Izcovich, Carlos A. Cuello-Garcia, Chen Chen, David J. Harris, Ewa Borowiack, Fatimah Chamseddine, Finn Schünemann, Gian Paolo Morgano, Giovanna E.U. Muti Schünemann, Guang Chen, Hong Zhao, Ignacio Neumann, Jeffrey Chan, Joanne Khabisa, Layal Hneiny, Leila Harrison, Maureen Smith, Nesrine Rizk, Paolo Giorgi Rossi, Pierre AbiHanna, Rayane El-khoury, Rosa Stalteri, Tejan Baldeh, Thomas Piggott, Yuan Zhang, Zahra Saad, Assem Khamis, and Marge Reinap. Physical distancing, face masks, and eye protection to prevent person-to-person transmission of SARS-CoV-2 and COVID-19: a systematic review and meta-analysis. *The Lancet*, 395(10242):1973–1987, 2020.
- [46] JS Turner. Turbulent entrainment: the development of the entrainment assumption, and its application to geophysical flows. *Journal of Fluid Mechanics*, 173:431–471, 1986.